Eur. Phys. J. B **30**, 17–23 (2002)
DOI: 10.1140/epjb/e2002-00353-0

THE EUROPEAN PHYSICAL JOURNAL B

Quantitative roughness of sputtered Fe-Cr superlattices

M.E. Gómez[1,a], J. Santamaria[1,b], M.C. Cyrille[2,c], E.C. Nelson[2], K.M. Krishnan[2], and I.K. Schuller[1]

[1] Department of Physics, University of California-San Diego, La Jolla, CA 92093-0319, USA
[2] Materials Sciences Division, National Center for Electron Microscopy, Lawrence Berkeley Laboratory, University of California, Berkeley, CA 94720, USA

Received 13 June 2002
Published online 19 November 2002 –

Abstract. We obtained quantitative values of all significant parameters describing the roughness of Fe-Cr superlattices, both in the lateral and growth directions, by statistical analysis of energy-filtered transmission electron microscopy images using cross section samples. These results are in good agreement with the complementary low-angle X-ray scattering measurements. The interface roughness of sputtered Fe-Cr superlattices was changed systematically by varying Ar-pressure during the growth and the number of the bilayers. By scaling local window size we obtained the dependence of the saturated roughness and its correlation lengths in both the lateral and growth directions. The roughness and its correlation lengths (lateral and perpendicular) increase with pressure. However correlation length in the lateral is constant with bilayer index for low-pressure sputtered samples

PACS. 68.35.Ct Interface structure and roughness – 68.65.Cd Superlattices – 68.37.Lp Transmission electron microscopy (TEM) – 61.10.Eq X-ray scattering

1 Introduction

It is well known that roughness determines important physical properties of thin films and superlattices through their dependence of the detailed atomic arrangement at surface and interfaces. Metallic superlattices composed of alternating magnetic and non-magnetic layers showing giant magneto resistance (GMR) [1], are critically affected by interfacial roughness [2]. Non-conformal roughness may cause layer thickness fluctuations of the non-magnetic layer, which may reduce (or destroy) antiferromagnetic (AF) alignment [3]. On the other hand, interface roughness may directly influence the spin dependent transport through modification of the electronic structure and/or change of the asymmetry of the interfacial contribution to the spin dependent scattering. A detailed characterization of the interface roughness at various length scales is of critical importance to clarify its influence on the GMR effect.

Roughness depends strongly on growth conditions and deposition parameters, in a way not yet well understood, mainly due to the non-thermodynamic growth conditions of most deposition techniques. For single films, significant effort has been devoted to understand the growth mechanism and its relation with surface roughness. Surface roughness has been characterized mainly by surface probe microscopy such as STM [4] and AFM [5,6], synchrotron sources X-ray scattering [7] and neutron reflectivity [8]. Existing theories of non-specular X-ray scattering assume [8,9] a Gaussian distribution of interface heights and an exponential decay of the height-height correlation function (self-affine surface). In many single films the roughness increases with lateral system size and thickness, following power laws with related exponents [10]; however, applying these concepts to superlattices is not straight forward, since kinetic roughening can be affected by having more than one constituent [11]. An important question is whether the roughness is replicated from layer to layer and how it advances from one interface to the other. An experimental characterization of the nature of the roughness, therefore, requires probing individual (buried) layers. Scanning probe microscopes require complicated experimental set ups to allow sequential *in situ* characterization of the interfaces and most importantly, interrupting the growth for the measurement which may alter growth kinetics.

X-ray diffraction (XRD) and TEM using cross-section samples are the two most commonly used complementary techniques to *ex situ* characterize superlattices [12]. Both techniques provide information averaged over different length scales: XRD averages over the structural coherence length, which is limited by grain size and roughness; TEM averages over the path length of the electrons through the sample.

XRD is an easy to use non-destructive, powerful structural analysis technique with a high penetration depth,

[a] On leave from Universidad del Valle, Cali, Colombia
e-mail: megomez@calima.univalle.edu.co
[b] On leave from Universidad Complutense, Madrid, Spain
[c] *Present address*: IBM Almaden, San José, California

which allows probing the whole superlattice structure. A major drawback of this technique is that the structural information is averaged over the whole superlattice stack, therefore, assumptions are made on the nature of the roughness and its replication from layer to layer. Extracting quantitative information on atomic positions thus requires fitting diffraction spectra to structural models. This we have done quite successfully for a number of years using the SUPREX refinement method [13].

Since Fe and Cr have similar lattice parameters and exhibit very close elastic scattering factors for electrons, conventional diffraction or phase-contrast imaging in a TEM will neither resolve the layers nor the details of their interface structure. To overcome this problem analytical tools are necessary to obtain element specific information. Energy Filtered Transmission Electron Microscopy (EFTEM) is a complementary technique to characterize roughness at nanometer scale. Cross-section samples provide direct images of each layer, allows probing directly the roughness, its lateral length scale and replication from layer to layer. A problem with this technique is that the 2D-roughness is projected along the cross section thickness into a one-dimensional profile. This problem has been analyzed previously [14] and is known to cause an underestimate of the roughness when compared with that extracted from X-ray diffraction. Here, on the other hand the roughness length scale is comparable or larger than the cross section thickness. Thus our conclusions are free from artifacts due to the projection effect. Additionally, the EFTEM sample thickness is much smaller than the mean free path for multiple scattering and the inelastic scattering events, such as the Fe and Cr $L_{2,3}$ edges, are strongly localized at atomic sites.

In this paper, we examine dc-sputtered Fe-Cr superlattices in which the roughness is varied in a controlled manner [15,16]. We use energy filtered electron energy loss spectroscopy digitized images in the cross sectional geometry to extract the roughness and its lateral correlation length for the individual layers. Results are compared with those obtained from the refinement of specular XRD patterns using the SUPREX [13] software, although each technique provides information over a limited and specific spatial range. We show that for samples produced at low sputtering pressure (5 mTorr) the roughness increases with increasing number of bilayers (17–40), but its lateral length scale remains constant. On the other hand, for samples with a constant number of bilayers, increasing sputtering pressure results in an increase of roughness and its lateral length scale. The ability of producing samples with controlled (and well-characterized) roughness, provides an avenue for a better understanding of the interfacial contribution to the GMR mechanism [17–19].

2 Experimental

Our study has been conducted on DC sputtered Fe-Cr superlattices sandwiched between a bottom and a top 100 nm thick Nb electrodes for transport measurements in the Current Perpendicular to the Plane (CPP) geometry. Two sets of samples were grown: the first set was grown varying the number of bilayers between 17 and 40 keeping the pressure at 5 mTorr; the second set was deposited varying pressure between 4 and 10 mTorr keeping constant the number of bilayers at 20. The Nb-layers were always grown at an Ar-pressure of 3 mTorr and with the same thickness to ensure that the Nb-buffer layer had always the same roughness. A detailed description of the growth, transport measurements and limited structural characterization has been reported elsewhere [15,16].

The superlattice structure was thoroughly characterized by low angle X-Ray diffraction using a Rigaku rotating anode diffractometer with $Cu-K_\alpha$ radiation. To estimate the interfacial roughness of the layers, the specular spectra were analyzed with the SUPREX refinement program. A structural model [13] was used with an increasing roughness with the bilayer index n according to a power law $\sigma_n = \sigma_{int} + \sigma_a n^\alpha$, where σ_a is the roughness of the first bilayer, σ_{int} an intrinsic roughness of the layers and α an exponent describing the evolution of the roughness.

Electron microscopy was carried out using a Philips CM20-FEG TEM equipped with a Gatan Imaging Filter, capable of obtaining both electron energy-loss spectra and energy-filtered images in real time at high spatial resolution. Samples suitable for imaging by TEM were prepared in the cross-section geometry following customary treatment of polishing, dimpling and low angle (less than 10 degree) ion milling to get large electron transparent regions thin enough for Electron Energy Loss Spectral (EELS) investigations without any multiple scattering.

Energy-filtered imaging techniques (after removal of the background due to other loss processes) were carried out on cross sectional images to show the Fe or Cr elemental maps at sufficient resolution to quantify the local structural roughness at the Fe-Cr or Cr-Fe interfaces. Two different methods (three windows or jump ratio method) were used to account for the effects of the non-characteristic background [20]. For each element three images were taken: two adjacent windows (A, B) with energies below the edge onset and, a third image in a window, labeled as C, corresponding to the characteristic edge. The images (A, B) were used to extrapolate the background under the characteristic edge and labeled as image D. Two different images C-D (three window method) and C/B (jump ratio method) were thus obtained independent of background effects. The digitized images were analyzed with help of the Gatan-Digital-Micrograph software to obtain Cr-Fe profiles. The pixel size for all samples was maintained at 0.27 nm. Intensity profiles along the growth direction were laterally averaged over 2.70 nm wide windows. This integration width was a compromise between having a signal- intensity sufficiently large to localize the maximum positions within the pixel uncertainty (0.27 nm, pixel size) and having this information for the maximum number of data points along the multilayer lateral direction for good statistical information.

Profiles showing the maximum Cr (Fe) intensity were constructed with a lateral spacing of 1.35 nm (5 pixels).

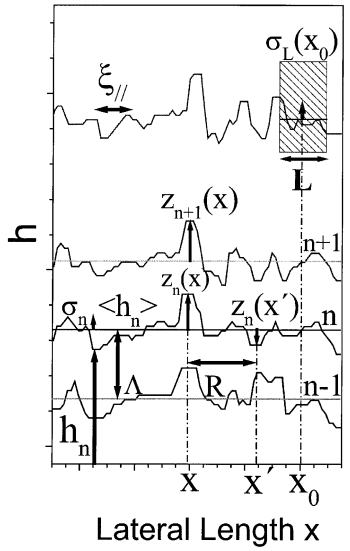

Fig. 1. Schematic diagram showing some bilayer profiles for a superlattice. The growth direction is shown along the y-coordinate and the lateral length along the x-coordinate. n describes the bilayer index. In this plot the bilayer profile height $h_n(x)$, its spatial averaged value $\langle h_n(x)\rangle_x$ (horizontal lines), height deviation $z_n(x)$, standard deviation σ_n, lateral relative coordinate R, bilayer modulation length Λ, lateral roughness correlation length $\xi_{\|}$, local window size L, local roughness $\sigma_L(x_0)$, parameters used in the text, are shown schematically.

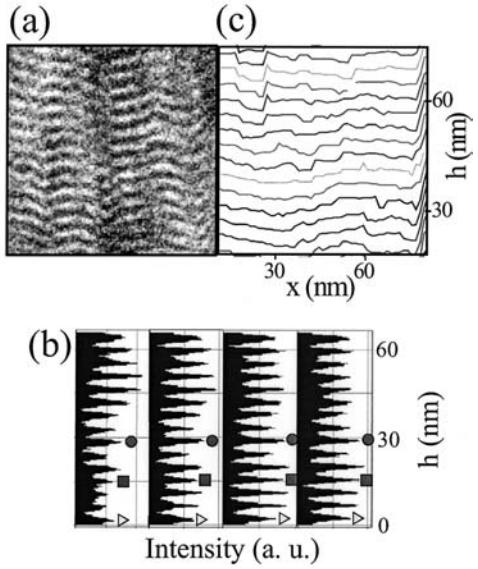

Fig. 2. (a) Typical Fe-map of $[\mathrm{Fe}(3\ \mathrm{nm})/\mathrm{Cr}(1.2\ \mathrm{nm})]_n$-superlattice grown at an Ar-pressure of 5 mTorr. (b) Fe-profiles for 4 different integration windows, h is the coordinate in the growth direction. Symbols ($\triangle, \square$, O) identify the position of height maxima for each bilayer. (c) Bilayer profiles for superlattice shown in micrograph (a). Figures (a) and (c) are on the same scale.

Since Cr and Fe profiles for the same bilayers were nearly identical, we will hereafter consider that the bilayer composition profile describes the interface. Digitized Fe (or Cr) profiles were then used to get the interface height $h_n(x)$ and the averaged value $\langle h_n(x)\rangle_x$ for each bilayer. n is the bilayer index and it takes values between 1 and N for the first and the last bilayer respectively. Figure 1 shows schematically such a superlattice, where h is the coordinate in the growth direction and the coordinate x the lateral length. The height deviations respect to an averaged value were used to define a height deviation function $z_n(x)$ as $z_n(x) = h_n(x) - \langle h_n(x)\rangle$ in terms of which the roughness $\sigma_n = [\langle z_n^2(x)\rangle]^{1/2}$ was analyzed statistically. Λ in Figure 1 corresponds to the superlattice modulation length.

3 Results and discussion

A typical EFTEM map in cross-section view of a sputtered $[\mathrm{Fe}(3\,\mathrm{nm})/\mathrm{Cr}(1.2\,\mathrm{nm})]_n$ superlattice is shown in Figure 2a. The bright intensity is proportional to the intensity of the Fe-characteristic $L_{2,3}$ energy-loss signal; dark regions mean absence of Fe. Typical Fe-profiles for a 2.7 nm wide integration window are shown in Figure 2b, where h represents the coordinate in the growth direction. Each integration window is laterally separated from the following one by 1.35 nm (5 pixels). From the position of each Fe(Cr)-maximum, represented in (b) by the symbols triangle-up, square and circle, and moving the integration window along the lateral direction, coordinate x, we get the bilayer-profiles. Figure 2c plots the positions of the maxima for each individual bilayer $h_n(x)$ as a function of the coordinate x.

Fe(Cr)-maps of a $[\mathrm{Fe}(3\ \mathrm{nm})/\mathrm{Cr}(1.2\ \mathrm{nm})]_n$-superlattices are shown in Figures 3 a to c for samples grown at 4, 5 and 10 mTorr respectively. Micrographs (a) and (c) correspond to the series of $\mathrm{Nb}(100\ \mathrm{nm})/[\mathrm{Fe}(3\ \mathrm{nm})/\mathrm{Cr}(1.2\ \mathrm{nm})]_{20}/\mathrm{Nb}(100\ \mathrm{nm})$, samples grown at different pressures (20 bilayers); Figure 3b corresponds to the series of $\mathrm{Nb}(100\ \mathrm{nm})/[\mathrm{Fe}(3\ \mathrm{nm})/\mathrm{Cr}(1.2\ \mathrm{nm})]_{40}/\mathrm{Nb}(100\ \mathrm{nm})$, multilayers grown at the same pressure (5 mTorr) varying the number of bilayers.

To get a quantitative evaluation of the interface roughness we have analyzed the height fluctuations $z(x)$, height differences $\Delta z(R)$, bilayer modulation length Λ as shown in Figures 4a, b, and c respectively for the sample grown at 4 mTorr. R is the lateral distance between points at which height is calculated, shown schematically in Figure 1. The statistical distributions of the height-differences $\Delta z(R)$ for the sputtered sample grown at 8 mTorr for different R-values are shown in Figures 4d, e, and f. The height difference forms a Gaussian distribution and its Full Width at Half Maximum (FWHM) increases with increasing relative coordinate R. This is a central assumption made in diffuse XRD experiment to quantitatively analyze roughness [4,5,8,9]. These EFTEM digitized multilayer maps provide a direct proof of the random Gaussian distribution of heights ($z(R)$) and height differences ($\Delta z(R)$) for each individual bilayer or collectively for all of them. This point was verified for all samples.

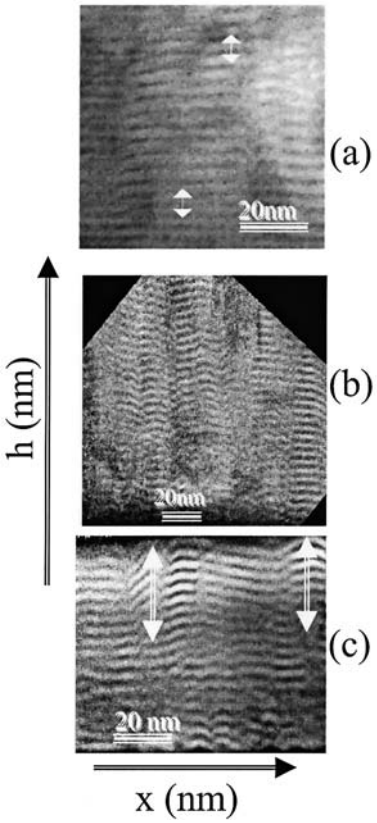

Fig. 3. Energy filtered Fe $L_{2,3}$ maps of [Fe(3 nm)/Cr(1.2 nm)]$_n$-superlattices. (a) Bilayers 3rd to 19th (4 mTorr); (b) bilayers 6th to 38th (5 mTorr); (c) bilayers 1st to 18th (10 mTorr). Arrows in (a) and (c) show the replication distance of small bumps and large bumps respectively. Scales in the growth direction are the same as that drawn over the micrograph in the lateral direction.

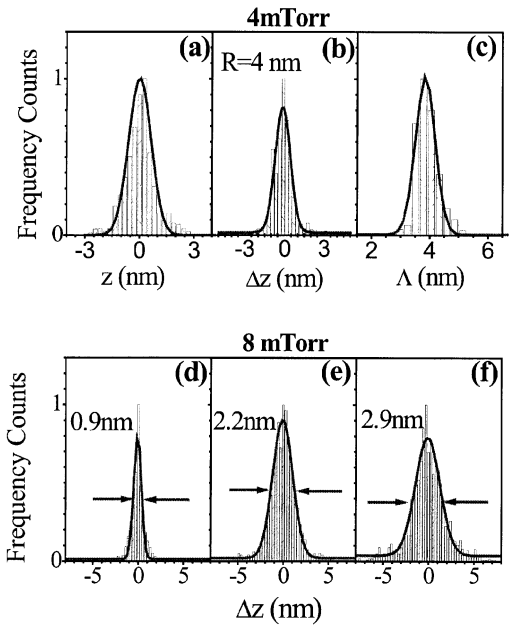

Fig. 4. Statistical plots of: (a) height function $z(x)$, (b) height difference $\Delta z(R) = z(x) - z(x+R)$ for $R = 4$ nm, (c) bilayer modulation length Λ for an [Fe(3 nm)/Cr(1.2 nm)]$_{20}$ superlattice grown at 4 mTorr. Statistical plots of the height differences $\Delta z(R)$ for: (d) $R = 1.35$ nm, (e) $R = 4$ nm, (f) $R = 6.7$ nm for an [Fe(3 nm)/Cr(1.2 nm)]$_{20}$ superlattice grown at 8 mTorr. FWHM, indicated by arrows are 0.9, 2.2 and 2.9 nm respectively.

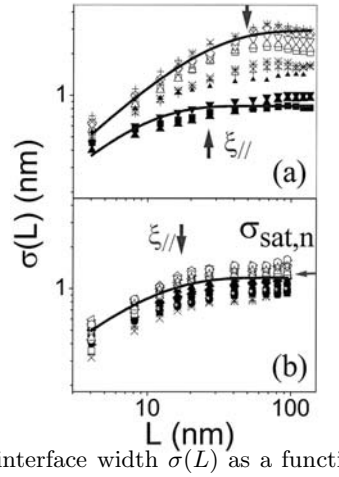

Fig. 5. Local interface width $\sigma(L)$ as a function of the local window width L for [Fe(3 nm)/Cr(1.2 nm)]$_{20}$ superlattices. (a) Sample grown at 8 mTorr-bilayers 1st to 18th. (b) sample grown at 5 mTorr-bilayers 8th to 34th. Data sets correspond to different bilayer index. The vertical arrows indicate the values of the lateral roughness correlation length $\xi_\parallel$ obtained from the fit. The horizontal arrow in (b) indicates the saturated roughness $\sigma_{sat,n}$ also obtained from the fit.

The lateral roughness correlation length $\xi_\parallel$ is defined as the lateral length over which the interface heights are correlated [10], see Figure 1. The most common procedure to obtain $\xi_\parallel$ is to analyze layer profiles for increasing lateral system size. Since EFTEM maps are not available over a wide range of image sizes, it is useful to study the scaling of the local roughness with window width [10]. The roughness for a window of size L around point x_0 is defined as $\sigma_L(x_0) = [\langle [z(x) - \langle z(x)\rangle_L]^2\rangle_L]^{1/2}$, where the averaging $\langle z(x)\rangle_L$ is done over the lateral window size L; x-values are within the window size L, as shown in the sketch of Figure 1. The size dependent roughness or local roughness width $\sigma(L)$ is obtained by averaging the local roughness $\sigma_L(x_0)$ over all available x-coordinates: $\sigma(L) = \langle \sigma_L(x_0)\rangle_x$. Figure 5 shows the variation of the lateral size dependent roughness $\sigma(L)$ as a function of the lateral window width L for individual bilayers, for (a) 8 mTorr sample with $N = 20$ bilayers and (b) sample grown at 5 mTorr with $N = 40$. Symbols change with bilayer index: first bilayers solid, last bilayers open.

The roughness increases with lateral window size L according to a power law ($\sigma(L) \sim L^\alpha$), then saturates. The position of the knee at saturation is a measure of the lateral correlation length $\xi_\parallel$ of the roughness. $\xi_\parallel$ is extracted from fits of the size dependent roughness for each bilayer to the expression:

$$\sigma_n(L) = \sigma_{sat,n}\left[1 - \exp(-(L/\xi_\parallel)^{2\alpha}\right]^{0.5}$$

where $\sigma_{sat,n}$ is the saturation value of the roughness for bilayer n, α is the roughness exponent [10]. Lines in Figures 5a and b are fits to this expression, which

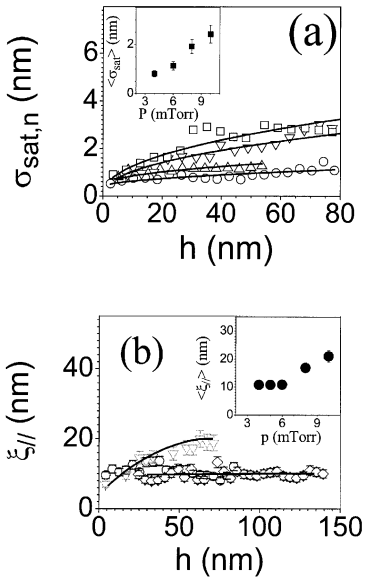

Fig. 6. (a) Evolution of the saturated roughness with height h for [Fe(3 nm)/Cr(1.2 nm)]$_{20}$ superlattices at 4 (O), 6 ($\triangle$), 8(∇) and 10 ($\square$) mTorr. Inset shows the dependence of $\langle\sigma_{sat}\rangle$ with pressure. (b) Evolution of the lateral roughness correlation length $\xi_{\parallel}$ as function of the height h for sputtered samples at 4 (O), 5 ($\Diamond$), 8 (∇) mTorr. The inset shows the dependence of the averaged value of $\langle\xi_{\parallel}\rangle$ with pressure.

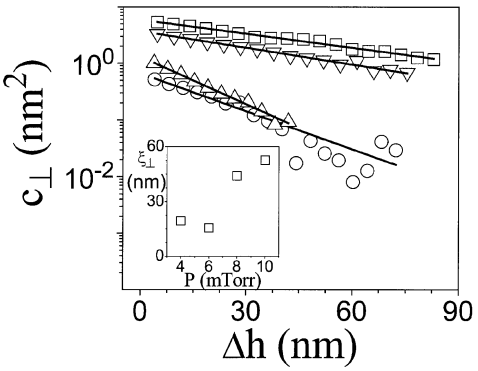

Fig. 7. The height-height correlation function in the growth direction $c_{\perp}$, as a function of vertical distance Δh for [Fe(3 nm)/Cr(1.2 nm)]$_{20}$ superlattices grown at 4 (O), 6($\triangle$), 8(∇) and 10($\square$) mTorr. The inset shows the dependence of the roughness correlation length in the growth direction $\xi_{\perp}$ as a function of pressure.

has the asymptotic behaviors $\sigma(L \ll \xi_{\parallel}) \approx L^{\alpha}$, and $\sigma(L > \xi_{\parallel}) \approx \sigma_{sat}$. The roughness exponent α is 0.75 ± 0.05 for the high-pressure sputtered samples (8 and 10 mTorr) and 0.65 ± 0.05 for the low-pressure sputtered samples (4, 5, 6 mTorr).

In Figure 6a, we display the saturation value of the roughness $\sigma_{sat,n}$ as a function of position in the growth direction h, for four different pressures (4, 6, 8 and 10 mTorr). These plots show that the roughness increases: a) with pressure; b) with h (or the bilayer index, n); c) and it is more pronounced for the high than the low-pressure samples. The lines in the figure are the results obtained from the refinement of the specular low angle X-ray diffraction patterns using the SUPREX software. The inset shows the saturation roughness averaged over the whole superlattice stack as a function of pressure. Samples were the same used for EFTEM analysis and similar to the ones used for the perpendicular transport measurements [15,16]. It is worth noting that there is very good agreement between the results of both techniques (XRD and EFTEM) although they average roughness on different length scales.

Figure 6b shows the lateral roughness correlation length $\xi_{\parallel}$ as a function of film thickness h (h is equivalent to bilayer index). $\xi_{\parallel}$ is nearly independent of bilayer index n for the low-pressure samples grown at 4 and 5 mTorr; but it increases with n in the high-pressure samples. Note that for the 5 mTorr sample (40 bilayer), $\xi_{\parallel}$ is constant with bilayer index up to the 36th bilayer. However, the roughness increases with the bilayer index in the high-pressure samples [15]. This behavior can be readily seen in the projected chemical maps of Figure 3. The lateral size of *bumps* in the bilayer profiles increase with bilayer index for the high-pressure samples, image (c) in Figure 3, but is constant for the 5 mTorr – 40 bilayers sample, image (b). The inset in Figure 6b shows that the averaged (over all layers) lateral correlation length $\langle\xi_{\parallel}\rangle$ increases with increasing pressure. Note that the roughness length scale (10–20 nm) is comparable to the cross section thickness used in the EFTEM measurements. Consequently artifacts due to the projection of the 2D-roughness pattern onto the 1D-bilayer profiles are minimal. In addition, the values obtained for the lateral correlation length (in the 10–20 nm range) are in agreement with previous reports for the same kind of samples based on diffuse X-ray scattering [21].

Since the roughness values are a significant fraction of the total bilayer thickness, the question arises whether the bilayer thickness is preserved over the multilayer stack. The bilayer period can be statistically analyzed for the individual bilayers to examine the evolution of the bilayer period and their fluctuations with the bilayer index. This analysis shows that the mean value of the bilayer thickness is preserved over the multilayer stack although the roughness of the last bilayer is larger than 1 nm and the thickness fluctuations do not change with the bilayer index either. We have reported earlier that high-pressure samples show larger bilayer thickness fluctuations than low-pressure ones [16].

The roughness replication can be analyzed using the digitized bilayer profiles. This is usually accomplished in terms of the height-height correlation function in the growth direction

$$c_{\perp}(h) = \langle z_n(x) z_{n+\Delta h}(x) \rangle_{x,n}$$

defined as the product of the heights z for the same x-coordinate of bilayers spaced Δh vertically (see Fig. 1) and averaged over all the available x-*values* and all the bilayers. Figure 7 shows a semi-log plot of the height-height correlation function $c_{\perp}$ as a function of the vertical distance Δh

in nm. Straight lines indicate an exponential decay of the correlation function $c_\perp(\Delta h)$ in the growth direction according to the expression $\exp(-(\Delta h/\xi_\perp)^{2\alpha})$, with $2\alpha = 1$. The slope provides a measure of the correlation length $\xi_\perp$ in the growth direction. The inset in Figure 7 shows the pressure dependence of the correlation length $\xi_\perp$, indicating longer $\xi_\perp$ for high than for low-pressure samples. This is in agreement with observations reported previously [11] *i.e.*, that large rough features are better replicated than small ones. We can see readily this behavior in the micrographs shown in Figure 3 where the replication distance of small (Fig. 3a) and large bumps (Fig. 3b) is marked by arrows. It is interesting to note that, since the average size of surface bumps is larger in high than in low-pressure samples ($\xi_\parallel$ increases with pressure), the lateral scale of the roughness dictates its replication properties in the vertical direction.

Roughness correlation in the growth direction has a direct implication for the AF alignment. In low-pressure samples the correlation length $\xi_\perp$ (around 20 nm) is smaller than the multilayer thickness (84 nm). This probably explains a substantial fraction of the ferro magnetically aligned material in these samples ($M_R/M_S \cong 0.6$) [16]. Although, we cannot make a definite statement on how the roughness (of the order of 1 nm in these samples) is shared between the Fe and Cr layers, one has to keep in mind, that a 0.2 nm Cr layer thickness fluctuation is enough to destroy the AF-coupling between the Fe layers. When pressure increases, the roughness increases considerably (2.4 nm for the 10 mTorr sample), but so does $\xi_\perp$ (50 nm for the 10 mTorr sample). Although the roughness is twice the thickness of the Cr layer, there is still a significant fraction of the sample that is coupled antiferromagnetically ($M_R/M_S \cong 0.8$).

Roughness has important implications for the transport properties. Transport measurements have been conducted in zero magnetic field and in magnetic fields of 1 T applied parallel to the layers to obtain the giant magnetoresistance in these samples. Results can be found in references [15,16,19]. Interestingly while the magnetoresistance ($\Delta\rho$) increases with interface width, the resistivity at saturation scales with the roughness lateral correlation length [19]. Samples produced at low pressure (5 mTorr) increasing the number of bilayers from 10 to 60 show an increasing average roughness but an almost constant roughness lateral correlation length. For these samples the saturation resistivity does not change with the number of bilayers. On the other hand in samples produced at increasing pressures (6–10 mTorr), the roughness increases and so does its lateral correlation length and an increase is also observed in the saturation resistivity [19].

In summary, we have used XRD and EFTEM in a quantitative evaluation of interface roughness parameters of sputtered Fe-Cr superlattices. A statistical analysis of EFTEM images provides quantitative information on the roughness of the individual layers. Roughnesses averaged over the whole superlattice stack are in very good agreement with values obtained from XRD. We have directly proven the Gaussian nature of the layer thickness fluctuations in this system. Additionally, EFTEM provides lateral and perpendicular roughness correlation lengths (which can not be obtained from X-ray analysis). We have shown that roughness can be modified with the growth parameters. For samples with a constant number of bilayers, increasing pressure results in an increase of both the roughness and its lateral correlation length. On the other hand for samples produced at low pressures (5 mTorr), an increase of the number of bilayers (up to 40) result in a moderate increase of the roughness but its lateral correlation length remains constant. The possibility of varying roughness parameters independently should provide an avenue for the understanding of their influence on the perpendicular magnetotransport in these structures [19], in which the importance of the interfacial roughness is particularly critical.

DOE supported this research. M.E. Gómez thanks COLCIENCIAS and Universidad del Valle for support of this research. J. Santamaria and I.K. Schuller thank the New Del Amo Program for international travel. Work at NCEM/LBL was supported by DOE/BES under contract number DE-ACO3-76SF00098.

References

1. M.N. Baibich, J.M. Broto, A. Fert, F. Nguyen Van Dau, F. Petroff, P. Etienne, G. Creuzet, A. Friederich, J. Chazelas, Phys. Rev. Lett. **61**, 2472 (1988)
2. For a review see for example Ivan K. Schuller, S. Kim, C. Leighton, J. Magn. Magn. Mater. **200**, 571 (1999)
3. T. Salditt, T.H. Metzger, J. Peisl, Phys. Rev. Lett. **73**, 2228 (1994)
4. H. You, R.P. Chiarello, H.K. Kim, K.G. Vandervoort, Phys. Rev. Lett. **70**, 2900 (1993)
5. J. Krim, G. Palasantzas, Int. J. Mod. Phys. B **9**, 599 (1995)
6. R. Paniago, H. Homma, P.C. Chow, S.C. Moss, Z. Barnea, S.S.P. Parkin, D. Cookson, Phys. Rev. B **52**, R17502 (1995)
7. W. Weber, B. Lengeler, Phys. Rev. B **46**, 7953 (1992); G. Palasantzas, J. Krim, Phys. Rev. B **48**, 2873 (1993); D.E. Savage, J. Kleiner, N. Schimke, Y.P. Phang, T. Jankowski, J. Jacobs, R. Kariotis, M.G. Lagally, J. Appl. Phys. **69**, 7411 (1991)
8. S.K. Sinha, E.B. Sirota, S. Garoff, H.B. Stanley, Phys. Rev. B **38**, 2297 (1988)
9. X. Yan, T. Egami, Phys. Rev. B **47**, 2362 (1993); G. Palasantzas, Phys. Rev. B **48**, 14472 (1993)
10. A.L. Barabasi, H.E. Stanley, in *Fractal Concepts in Surface Growth* (Cambridge University Press, Cambridge, 1995)
11. Y.H. Phang, D.E. Savage, R. Kariotis, M.G. Lagally, J. Appl. Phys. **74**, 3181 (1993); R. Paniago, R. Forrest, P.C. Chow, S.C. Moss, S.S.P. Parkin, D. Cookson, Phys. Rev. B **56**, 13442 (1997)
12. E.E. Fullerton, W. Cao, M.J. Carey, I.K. Schuller, A.E. Berkowitz, Appl. Phys. Lett. **63**, 1 (1993)

13. I.K. Schuller, Phys. Rev. Lett. **44**, 1597 (1980); W. Sevenhans, M. Gijs, Y. Bruynseraede, H. Homma, I.K. Schuller, Phys. Rev. B **34**, 5955 (1986); E.E. Fullerton, I.K. Schuller, H. Vanderstraeten, Y. Bruynseraede, *ibid.* B **45**, 9292 (1992); D.M. Kelly, E.E. Fullerton, J. Santamaria, I.K. Schuller, Scripta Met. Mat. **33**, 1603 (1995)
14. Y. Lepetre, E. Ziegler, I.K. Schuller, Appl. Phys. Lett. **50**, 1480 (1987)
15. M.C. Cyrille, S. Kim, M.E. Gómez, J. Santamaria, K.M. Krishnan, I.K. Schuller, Phys. Rev. B **62**, 3361 (2000)
16. M.C. Cyrille, S. Kim, M.E. Gómez, J. Santamaria, C. Leighton, K.M. Krishnan, I.K. Schuller, Phys. Rev. B **62**, 15079 (2000)
17. C.M. Schmidt, D.E. Bürgler, D.M. Schaller, F. Meisinger, H.J. Güntherodt, K. Temst, J. Appl. Phys. **89**, 181 (2001)
18. R.R. Gareev, D.E. Bürgler, M. Buchmeier, D. Olligs, R. Schreiber, P. Grünberg, Phys. Rev. Lett. **87**, 15702 (2001); A. Yoshihara, J.T. Wang, K. Takanashi, K. Himi, Y. Kawazoe, H. Fujimori, P. Grünberg, Phys. Rev. B **63**, 10405 (2001)
19. J. Santamaria, M.E. Gómez, M.C. Cyrille, K.M. Krishnan, I.K. Schuller, Phys. Rev. B **65**, 012412 (2002)
20. D.B. Williams, C.B. Carter, *Transmission Electron Microscopy IV Spectrometry* (Plenum Press, New York, 1996) and references therein; R.F. Egerton, *Electron Energy-Loss Spectroscopy in the Electron Microscope* (Plenum Press, New York 1996)
21. R. Schad, P. Belien, G. Verbanck, V.V. Moshchalkov, Y. Bruynseraede, H.E. Fischer, S. Lefebvre, M. Bessiere, Phys. Rev. B **59**, 1242 (1999)